

Hyperfine-to-rotational energy transfer in ultracold atom–molecule collisions of Rb and KRb

Received: 23 July 2024

Accepted: 13 February 2025

Published online: 7 April 2025

 Check for updatesYi-Xiang Liu^{1,2,3,7}, Lingbang Zhu^{1,2,3,7}, Jeshurun Luke^{1,2,3}, Mark C. Babin^{1,2,3}, Marcin Gronowski⁴, Hela Ladjimi⁴, Michał Tomza⁴, John L. Bohn⁵, Timur V. Tscherbul⁶ & Kang-Kuen Ni^{1,2,3}✉

Energy transfer between different mechanical degrees of freedom in atom–molecule collisions has been studied and largely understood. However, systems involving spins remain less explored. In this study, we directly observed energy transfer from atomic hyperfine to molecular rotation in the ^{87}Rb ($|F_a, M_{F_a}\rangle = |2, 2\rangle$) + $^{40}\text{K}^{87}\text{Rb}$ ($X^1\Sigma^+$, rotational state $N = 0$) \rightarrow Rb ($|1, 1\rangle$) + KRb ($N = 0, 1, 2$) collision with state-to-state precision. We also performed quantum scattering calculations that rigorously included the coupling between spin and rotational degrees of freedom at short range under the assumption of rigid-rotor KRb monomers moving along a single potential energy surface. The calculated product rotational state distribution deviates from the observations even after extensive tuning of the atom–molecule potential energy surface. In addition, our ab initio calculations indicate that spin–rotation coupling is enhanced close to a conical intersection that is energetically accessible at short range. This, together with the deviation, suggests that vibrational degrees of freedom and conical intersections play an important part in the coupling. Our observations confirm that spin is coupled to mechanical rotation at short range and establish a benchmark for future theoretical studies.

Advances in joint experimental and theoretical tools have allowed scattering experiments to probe molecular interactions during collisions, revealing reaction mechanisms, dynamics and the structures of collisional complexes^{1–4}. After decades of work, sophisticated and accurate quantum dynamics calculations of atom–molecule collisions are now feasible⁵, especially for collisions and reactions involving only vibrational, rotational and electronic states^{6–12}.

Adding spin degrees of freedom complicates the interactions and poses challenges for experiments and a full understanding of the dynamics. Yet, collisions involving spins are of interest in many areas, such as buffer gas cooling¹³, sympathetic cooling^{14–17}, spin-exchange optical pumping^{18,19}, Feshbach resonances^{20–23} and the

magneto-association of triatomic molecules²⁴. Another notable example is the spin–orbit interaction, which plays an important role in the paradigmatic chemical reaction $\text{F} + \text{H}_2 \rightarrow \text{HF} + \text{H}$, the only known source of HF in the interstellar medium^{25,26}.

Besides their fundamental significance, spin-dependent interactions could play an essential role in the formation of long-lived complexes in ultracold atom–molecule and molecule–molecule collisions^{27–29}. These complexes are commonly described using the statistical Rice–Ramsperger–Kassel–Marcus (RRKM) theory, which gives the lifetime (τ) of a complex as $\tau = 2\pi\hbar\rho/N_o$, where \hbar is the reduced Planck constant, ρ is the density of states and N_o is the number of open channels^{27,28}. While the lifetimes predicted by the RRKM theory agree

¹Department of Chemistry and Chemical Biology, Harvard University, Cambridge, MA, USA. ²Department of Physics, Harvard University, Cambridge, MA, USA. ³Harvard-MIT Center for Ultracold Atoms, Cambridge, MA, USA. ⁴Faculty of Physics, University of Warsaw, Warsaw, Poland. ⁵JILA, NIST and Department of Physics, University of Colorado, Boulder, CO, USA. ⁶Department of Physics, University of Nevada, Reno, NV, USA. ⁷These authors contributed equally: Yi-Xiang Liu, Lingbang Zhu. ✉e-mail: ni@chemistry.harvard.edu

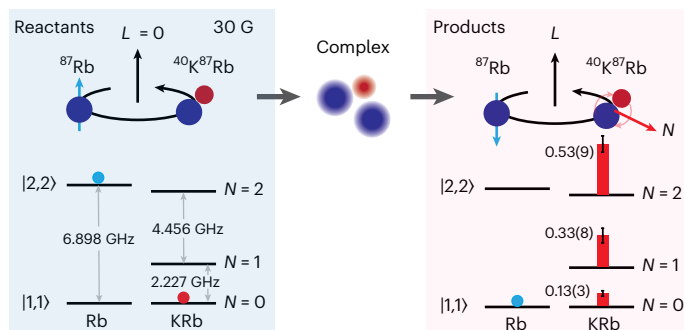


Fig. 1 | Schematic of hyperfine-to-rotational energy transfer in $^{87}\text{Rb} + ^{40}\text{K}^{87}\text{Rb}$ collisions. Left: Rb atoms were prepared in the $|F_a = 2, M_{F_a} = 2\rangle$ excited hyperfine state of the $5S_{1/2}$ manifold, while KRb molecules were prepared in the ground rotational state $|N = 0\rangle$ of their vibronic ground state, $X^1\Sigma^+$, $v = 0$, where v is the vibrational quantum number. L represents the collision partial wave between the atom and molecule. Right: following collision, Rb atoms relaxed to the $F_a = 1$ manifold, predominantly to the $|1, 1\rangle$ state, while the molecules populated multiple rotational states up to $N = 2$. The red bars represent the experimentally measured branching ratio. This process occurred due to coupling between atomic spin and molecular rotation in the KRb_2 collision complex. This collision was studied under external magnetic field $\mathbf{B} = 30\text{ G}$ and electric field $\mathbf{E} = 17\text{ V cm}^{-1}$, where \mathbf{B} and \mathbf{E} were perpendicular to one another.

well with some experiments, such as $\text{KRb} + \text{KRb}$ (ref. 30) and $\text{RbCs} + \text{RbCs}$ (ref. 31), this is not the case for other complexes^{32,33}. A striking example is the Rb–KRb collision complex formed by the Rb atom in the ground hyperfine state ($|F_a, M_{F_a}\rangle = |1, 1\rangle$), where F_a and M_{F_a} are the hyperfine quantum number and its projection along the quantization axis, and KRb is in its rovibronic ground state; the experimentally measured lifetime of this complex is five orders of magnitude longer than RRKM estimates in which spins were treated as ‘spectators’³⁴. At present, this discrepancy remains unsolved³⁵. Recently, ab initio evidence for strong spin-dependent hyperfine interactions was reported for the Rb–KRb complex³⁶. Because sufficiently strong spin-dependent interactions can couple electron and nuclear spins to molecular rotations at short range, spins can dramatically increase the density of states of ultracold collision complexes and hence their RRKM lifetimes^{27,29}, potentially explaining the large discrepancy.

These crucial spin-dependent hyperfine interactions have never been experimentally observed directly or rigorously explored in quantum scattering calculations. On the experimental side, detecting these interactions would require state-to-state measurements of collisional processes specifically mediated by spin-dependent interactions. On the theoretical side, enormous rotational and spin basis sets have prevented rigorous atom–molecule quantum scattering calculations³⁷.

In this study, we directly probed the spin-dependent interactions in Rb + KRb collisions by activating the spin degree of freedom with the Rb atom prepared in an excited hyperfine state ($|F_a, M_{F_a}\rangle = |2, 2\rangle$; Fig. 1). We also calculated the underlying potential energy surfaces and developed the formalism for rigorous quantum scattering calculations to model these collisions. As the $\text{KRb} + \text{Rb} \rightarrow \text{K} + \text{Rb}_2$ reaction is endothermic³⁴, only inelastic collision outcomes are allowed at ultracold temperatures. We directly measured the final states of the atoms and molecules, finding the excitation of molecules to all energetically allowed rotational levels commensurate with a relaxation of the atoms to their ground hyperfine states. This observation confirms the coupling between spin and mechanical rotation in the KRb_2 complex.

Results and discussion

The experiment started with a cloud of $10^{40}\text{K}^{87}\text{Rb}$ and 10^{487}Rb atoms co-trapped in an optical dipole trap (ODT) operating at a wavelength of 1,064 nm. The molecules were prepared in the rovibronic ground

state $X^1\Sigma^+ |N = 0, M_N = 0, M_{I,K} = -4, M_{I,\text{Rb}} = 1/2\rangle$, where N is the rotational quantum number, M_N is the rotation projection onto the magnetic field axis, $M_{I,K}$ and $M_{I,\text{Rb}}$ are the nuclear spin projections of K (nuclear spin $I_K = 4$) and Rb (nuclear spin $I_{\text{Rb}} = 3/2$) onto the magnetic field axis at 0.4 μK following the procedure described previously^{38,39}. The Rb atoms were residuals from the Feshbach association process and were in the $|F_a, M_{F_a}\rangle = |1, 1\rangle$ state at 0.8 μK . Following molecule production, the magnetic field was ramped down from 543.5 G to 30 G in 20 ms, after which the Rb atoms were transferred from the $|1, 1\rangle$ state to the $|2, 2\rangle$ state via an adiabatic rapid passage microwave pulse. At this point, the atom–molecule collisions of interest began. The excess energy in this inelastic collision is carried away as the kinetic energy of the products, allowing for their escape from the ODT. The products were then probed via a state-selective $1 + 1'$ resonance-enhanced multiphoton ionization (REMPI) scheme (see ‘ $1 + 1'$ REMPI detection of collisional products’ in the Methods). In the experiment, we protected the reactant cloud from REMPI beams using a dark mask (see ‘ $1 + 1'$ REMPI detection of collisional products’ in the Methods) and only probed the escaping products of the collisions.

REMPI detection of collision products

To detect the hyperfine states of the product Rb atoms, we applied a 420 nm laser resonant with the $5S_{1/2}, F_a = 1$ to $6P_{3/2}$ transition and then photoionized the $6P_{3/2}$ Rb atoms using a 532 nm pulsed laser (Fig. 2a). The resulting Rb REMPI spectrum is shown in Fig. 2b along with theoretical stick spectra for transitions resulting from various M_{F_a} levels within $F_a = 1$. The stick spectra take into account the laser polarization and Clebsch–Gordan coefficients between different Zeeman states, which represent the ionization spectrum if all three M_{F_a} states are evenly populated. In the experiment, only lines corresponding to the $M_{F_a} = 1$ states were observed, with no signature lines of the $M_{F_a} = 0, -1$ states observed. This indicates that the atoms predominately (>95%) populate the $|1, 1\rangle$ state following collision. We similarly performed $F = 2$ to $6P_{3/2}$ spectroscopy and found that the population of $|2, 1\rangle$ is less than 5% of the total Rb population with negligible population in other M_{F_a} levels.

Similarly, we probed the rotational state of KRb molecules after collisions using the REMPI scheme shown in Fig. 2c. By scanning the 666 nm laser frequency, we identified KRb molecules in the $N = 0, 1$ and 2 states following collision (Fig. 2d). We found no evidence for KRb excited to the $N = 3$ level, suggesting that these rotationally excited KRb species originated from a single collisional event, as a secondary collision with a $|2, 2\rangle$ Rb atom would have sufficient energy to reach the $N = 3$ level (–6.683 GHz from $N = 2$).

To obtain a quantitative population distribution of the KRb rotational states, we scanned the delay t of the 532 nm pulsed laser with respect to the beginning of the 666 nm excitation pulse (Fig. 3). With a pulse delay time t , the ion counts are proportional to the population of $\text{B}^1\Pi$ after the first transition of the REMPI (Fig. 2c), which mainly depends on the molecule population in N , the 666 nm Rabi rate for each transition and the excited-state lifetime. For $N = 2$ and 1 , we observed a damped oscillation. The lineshape of the $N = 0$ scan showed little dependence on the delay t because the pulsed 532 nm beam induced a light shift in the $\text{R}(0)$ transition (see ‘ $1 + 1'$ REMPI detection of collisional products’ in the Methods) and the 666 nm pulse was resonant only for a fixed duration when the 532 nm beam was on.

Because the exoergicity of this inelastic collision is small, the product molecules are relatively slow moving and can experience multiple ionization pulses before they leave the detection region, while the REMPI efficiency for each ionization event varies as the ionization beam intensity decays following a Gaussian profile. To account for all these factors, we performed a Monte Carlo simulation of the multipulse ionization process and fitted the results to the data in Fig. 3 to extract the branching ratio (see ‘Monte Carlo simulation of REMPI’ in the Methods for details).

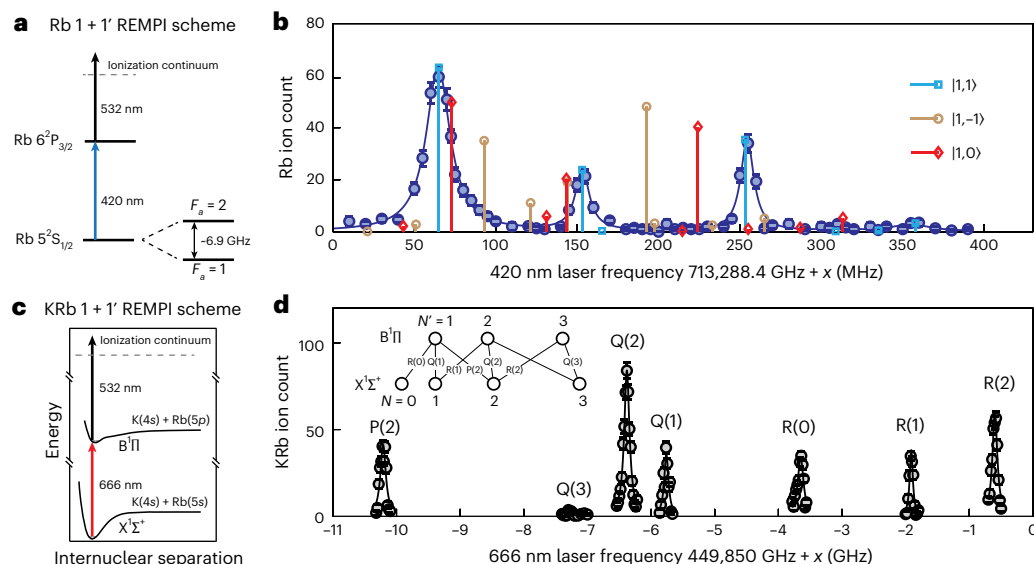


Fig. 2 | REMPI detection of collision products. **a**, Rb REMPI detection scheme. State-selective ionization of Rb was performed using a 1 + 1' REMPI scheme, with the 420 nm laser pulse resonant with the $5S_{1/2}$, $F_a = 1$ to $6P_{3/2}$ transition, followed by a 532 nm pulsed laser (10 ns) ionizing atoms in the $6P$ state. We note that two-photon ionization from the 532 nm laser was negligible compared with the REMPI process. **b**, Rb REMPI spectroscopy of the $|2, 2\rangle + \text{KRb}$ collision products. Filled blue circles represent data points. The solid dark-blue line represents a fit to Lorentzian line shapes. We extracted the 420 nm laser polarization composition from the relative heights of the Lorentzian peaks. Light-blue (open squares) vertical lines represent the predicted line positions for Rb atoms in the $|1, 1\rangle$ state in $5S_{1/2}$ targeting different hyperfine states in $6P_{3/2}$. Similarly, the red (open diamonds) and brown (open circles) vertical lines show the predicted line positions for $|1, 0\rangle$ and $|1, -1\rangle$ in $5S_{1/2}$, respectively. The vertical lines were simulated using the fitted polarization and assuming equal population among

the various M_{F_a} levels, scaled such that the population of $|1, 1\rangle$ matches the data. The data points represent the mean of three averages; the error bars represent the shot noise. **c**, KRb REMPI detection scheme. Rotational-state-selective ionization of KRb was performed using a 1 + 1' REMPI scheme, where the 666 nm laser pulse was resonant with one of the $X^1\Sigma^+$, $v = 0$, $N = 0, 1$ and 2 to $B^1\Pi$, $v' = 0$ rovibronic transitions, followed by a 532 nm pulsed laser directly ionizing KRb in the $B^1\Pi$ state. **d**, REMPI spectra of KRb collision products. The 666 nm laser frequency was scanned over 11 GHz, revealing a number of qualitative features corresponding to molecular rovibrational P ($\Delta N = N' - N = -1$), Q ($\Delta N = 0$) and R ($\Delta N = 1$) transitions of the $N = 0, 1$ and 2 levels of $X^1\Sigma^+$ KRb (circles). The solid lines are Lorentzian fits. Notably, no molecules were observed in the $N = 3$ level. Inset: Herzberg diagram of relevant transitions between the KRb ground and excited states⁴⁹. The data points represent the mean of five averages; the error bars represent the shot noise.

From the fitting, we obtained the number of molecules in each rotational state and determined the branching ratio for $N = 2, 1$ and 0 to be $0.53(9):0.33(8):0.13(3)$. The error bars were calculated by propagating a 68% confidence interval from the fitted molecule numbers and assuming a 10% overall fluctuation in the initial atom and molecule numbers. We also studied a $|2, 2\rangle$ Rb colliding with KRb in $N = 1$ and found that the population of the product KRb rotational states followed a branching ratio for $N = 2, 1, 0$ of $0.59(13):0.32(9):0.09(2)$ (Extended Data Table 1). This indicates that the scattering process is relatively insensitive to the interaction potential.

A pure chemical exchange channel, in which the incoming Rb atom swaps with the Rb atom in the KRb molecule, could qualitatively explain our observations. In the $|0, 0, -4, 1/2\rangle \text{KRb} + |2, 2\rangle \text{Rb}$ collision, the nuclear spin states of the two Rb atoms are different, allowing the Rb atom to end up in the $|1, 1\rangle$ state after exchange. To test whether chemical exchange alone could explain our results, we also studied KRb in $|0, 0, -4, 3/2\rangle$ and Rb in $|2, 2\rangle$, where both Rb atoms have the same nuclear spin state $M_{I,\text{Rb}} = 3/2$. We observed KRb in the $N = 2$ state after collision, indicating the coupling between atomic spin and mechanical rotation in the KRb_2 system, as a pure chemical exchange process would effectively result in an elastic collision.

Statistical aspects of Rb + KRb scattering

One way to interpret the observed Rb spin flip is to use a statistical theory of collision complexes and a time-dependent perturbation theory applied to the spins²⁷. We modelled the complex as a Rb atom repeatedly bouncing off the KRb molecule at a time interval estimated by averaging over classical trajectories in a pure C_6 potential. Given a typical gigahertz spin-dependent interaction strength³⁶ and a $0.54(10)$ ns measured complex lifetime (Supplementary Section D),

a single Rb spin flip probability is found to be near unity, while a second spin flip to $|1, 0\rangle$ is unlikely (see 'Rb spin-flip rate based on a statistical model' in the Methods), matching the observation.

The fact that the relative populations of the rotational states N are in proportion to their degeneracies $2N + 1$ invites a statistical interpretation of the branching ratios before diving into rigorous quantum scattering calculations. We calculated the expected KRb branching ratio assuming that the collision process is ergodic and that all states of the collision complex, as well as all exit channels, are populated with equal probability. In total, there are six angular momenta in the system: molecular rotation \hat{N} , collision partial wave \hat{L} , Rb atom nuclear spin \hat{I}_a , Rb electronic spin \hat{S} , K molecular nuclear spin \hat{I}_1 and Rb molecular nuclear spin \hat{I}_2 . As our method of detection can only resolve atom spins and molecular rotation, the molecular nuclear spins and partial wave enter into the degeneracies of the $N = 0, 1, 2$ product channels. When the external magnetic field is weak (our measurement at 2 G yields the same ratio as at 30 G, Extended Data Table 1), the total angular momentum \hat{J} is conserved. The total angular momentum \hat{J} is the vector sum of the angular momentum for total mechanical rotation $\hat{J}_r = \hat{N} + \hat{L}$ and the spin angular momentum $\hat{F} = \hat{S} + \hat{I}_a + \hat{I}_1 + \hat{I}_2$.

If we assume that all of the degrees of freedom are scrambled, the degeneracies of the $N = 2, 1, 0$ channels have a ratio of $0.544:0.340:0.116$ following the statistical model (see 'Statistical model of the KRb branching ratio' in the Methods), in agreement with the measured ratio.

We acknowledge that the spin-dependent interaction terms in the Hamiltonian are weak, in which case the total mechanical rotation angular momentum J_r would be conserved in the collision. Assuming the conservation of $J_r = 0$ throughout the process, the statistical model predicts the ratio of $N = 2, 1, 0$ to be 1:1:1, which deviates from the experimental finding. Thus, the statistical hypothesis can explain

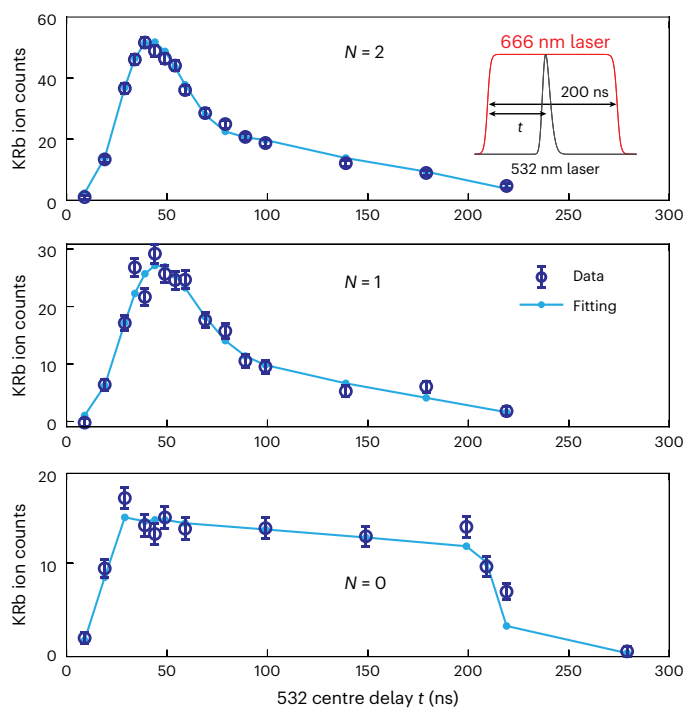


Fig. 3 | Extracting the KRb branching ratio. The relative time delay between the 666 and 532 nm REMPI pulses was scanned. The 666 nm laser was resonant with the Q(2) (top), Q(1) (middle) and R(0) (bottom) transitions. The pulse length of the 666 nm laser was fixed at 200 ns. Inset: powers of the REMPI beams as a function of time. The open circles are data points collected with 20 averages; the error bars represent shot noise. The filled circles connected by lines are fits to the Monte Carlo simulation. From the line shape, we can extract the Rabi rate of the three transitions and the population of molecules in the $N = 2, 1$ and 0 states after collision.

the observed distribution of rotational levels, provided that J_r is able to change freely during collision.

Rb + KRb interactions

As an alternative hypothesis to explain the distribution of rotational levels, we performed a full coupled-channel calculation.

We began by using ab initio quantum chemical methods to obtain the interaction potentials $V(R, r, \theta)$ in Jacobi coordinates (where R is the atom–molecule distance, r is the internuclear distance in KRb and θ is the orientation angle; Supplementary Section A), which dominate the atom–molecule collisions but do not couple spins. Examples of these potential energy surfaces (PESs) for selected geometries are presented in Fig. 4a.

These surfaces reveal various important facts about the interaction: (1) the Rb + KRb PESs are highly anisotropic, (2) the conical intersection (CI) between the ground and first-excited electronic states is energetically accessible for ultracold Rb + KRb collisions, (3) the excited electronic state is also energetically accessible at short range, (4) the excited-state PES is strongly dependent on the internuclear distance in KRb (that is, its vibration), while the ground-state PES shows little dependence on it, and (5) the exchange of Rb atoms can proceed without any electronic barrier.

In addition, we contemplated spin-dependent interactions that are active in the short range and that take the form

$$\hat{V}_{\text{sd}} = \sum_{m=1,2,a} \left[A_m^{\text{FC}}(R, r, \theta) \hat{\mathbf{S}} \cdot \hat{\mathbf{I}}_m + \hat{\mathbf{S}} \cdot A_m^{\text{ahf}}(R, r, \theta) \cdot \hat{\mathbf{I}}_m \right] + \hat{\mathbf{S}} \cdot \epsilon(R, r, \theta) \cdot (\hat{\mathbf{N}} - \hat{\mathbf{L}}). \quad (1)$$

The intermolecular hyperfine interactions between $\hat{\mathbf{S}}$ and $\hat{\mathbf{I}}_m$ consist of scalar Fermi contact couplings $A_m^{\text{FC}}(R, r, \theta)$ and tensor (or anisotropic

hyperfine, ahf) couplings $A_m^{\text{ahf}}(R, r, \theta)$ (ref. 40), which depend on the atom–molecule distance R , the internuclear distance r in KRb and the orientation angle θ . Finally, the spin–rotation interaction between the overall rotation of the collision complex and its electronic spin is described by the tensor $\epsilon(R, r, \theta)$. All of the terms in equation (1) depend on θ and couple spins to the mechanical rotation, which qualitatively explains the hyperfine-to-rotational energy transfer.

The Fermi contact interaction is generally the dominant spin-dependent interaction at short range, with typical values on the order of gigahertz (ref. 36), but conserves J_r . By contrast, the intermolecular spin–rotation and tensor hyperfine interactions in equation (1) couple states with different J_r , and so does the intramolecular nuclear electric quadrupole interaction in KRb, which is part of the KRb molecular Hamiltonian \hat{H}_{mol} (Supplementary Equation (4)). However, the spin–rotation coupling has a typical short-range value of around 10 MHz and is enhanced to gigahertz values at the CI (Fig. 4b). The typical strength of the tensor hyperfine is on the order of 10 MHz for the Rb–KRb complex, while the strength of the nuclear electric quadrupole interaction in KRb is less than 1 MHz (ref. 41).

Coupled-channel calculations

A complete quantum scattering calculation incorporating both electronic energy surfaces and molecular vibration, together with nuclear spins, molecular rotations and external fields, is not possible at present.

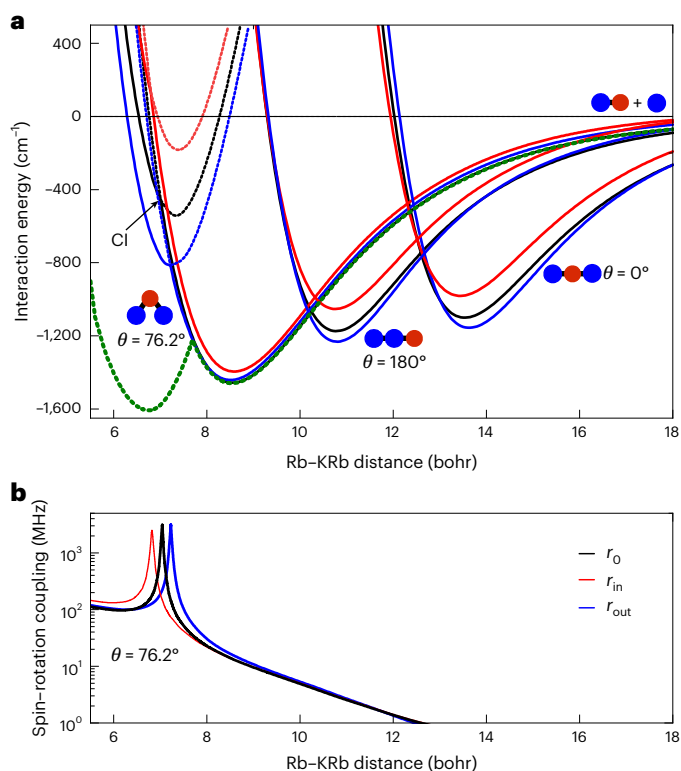


Fig. 4 | PESs and spin–rotation coupling of the Rb + KRb system. **a**, One-dimensional cuts through the three-dimensional electronic interaction potentials $V(R, r, \theta)$ for the ground (solid lines) and first-excited (dashed lines) electronic states. Three orientations θ are presented: two linear configurations ($\theta = 0^\circ$ and 180°) and one bent arrangement for which a conical intersection (CI) exists ($\theta_{\text{CI}} \approx 76.2^\circ$). Three intramolecular distances r in KRb were selected: the vibrationally averaged value r_0 and inner and outer classical turning points r_{in} and r_{out} , respectively, of the ground rovibronic level of KRb. The excited state of the linear geometries is outside the range of the plot. The green dotted line shows the ground-state interaction energy for θ_{CI} , minimized over r . **b**, Isotropic part of the spin–rotation coupling tensor $|\text{Tr}[\epsilon(R, r, \theta)]/3|$ corresponding to the geometries presented in **a**. The couplings for the linear geometries around their minima overlap with those for $\theta \approx 76.2^\circ$.

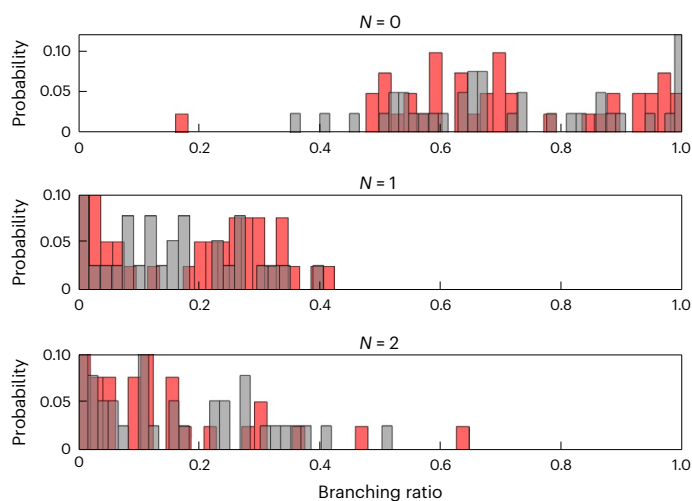


Fig. 5 | Histograms of rotational-state distributions of product KRb. KRb rotational-state population distributions following ultracold Rb ($|2, 2\rangle$) + KRb ($|0, 0, -4, 1/2\rangle$) collisions, obtained from converged CC calculations that included the 181 lowest rotational states of KRb and $J_r = 0$. The distributions are defined as state-to-state inelastic cross-sections to a given final rotational state of KRb (N) summed over all hyperfine sublevels in the N th manifold and normalized to the total inelastic cross-section. The distributions are averaged over 40 samples of PES2 (grey bars) and PES7 (red bars). The PES samples were obtained by scaling the corresponding PESs by a constant factor λ , as described in the Supplementary Information.

We therefore made the following assumptions (Supplementary Section B). First, the KRb fragment is assumed to be rigid, which is necessary to limit the number of scattering channels, and hence the computational complexity, to a tractable level. Second, the CI between the ground and first-excited electronic states of Rb–KRb is neglected for the same reason. Under these assumptions, we developed a coupled-channel (CC) model of Rb + KRb collisions in an external magnetic field based on the *ab initio* PES³⁶ and spin-dependent interactions (equation (1)). These approximations enabled us to rigorously account for all rotational and spin degrees of freedom of Rb–KRb in the presence of an external magnetic field. Our approach complements previous calculations on ultracold alkali dimer–atom collisions, which did not include spin degrees of freedom and Zeeman interactions, but rigorously treated the rovibrational modes and CIs^{42,43}.

To handle the computational complexity, we used a recently developed CC basis set composed of the eigenstates of the total mechanical rotational angular momentum of the atom–molecule system $\hat{J}_r = \hat{N} + \hat{L}$ (ref. 37). As shown in Supplementary Section B, our CC model, which rigorously includes all six angular momenta in Rb–KRb and the couplings between them, predicts that J_r is nearly perfectly conserved in the rigid-rotor approximation. In addition, to explore the role of the CI, we included in our CC calculations the spin–rotation tensor, which is greatly enhanced close to the CI (Supplementary Information). The calculations show that to break the conservation of J_r , the already enhanced spin–rotation interaction would have to be inflated by a factor of ≥ 100 . This indicates that the effects of vibrational modes and the CI go beyond just enhancing the spin–rotation interaction and need to be accounted for in a more rigorous way, such as explicitly including them in CC calculations in the future.

The fact that J_r is conserved in the CC model greatly reduces the computational cost. Using extensive basis sets, including as many as 181 rotational states of KRb, we demonstrated numerical convergence of Rb + KRb collision cross-sections in the rigid-rotor approximation. This marks the achievement of convergence for a heavy, strongly anisotropic atom–molecule collision system in a magnetic field including the rotational and spin degrees of freedom.

To account for the variation in the final product state distributions with respect to the fine details of the PES, we averaged the calculated distributions over 40 PES samples⁴⁴. The resulting histograms (Fig. 5) show that the product KRb rotational states tend to peak in the lowest final rotational state $N = 0$, in disagreement with experiment. The corresponding Rb product state distribution is largely dominated by the $|F_a = 1, M_{F_a} = 1\rangle$ and $|F_a = 2, M_{F_a} = 1\rangle$ hyperfine states, consistent with the selection rules for spin-dependent interactions in equation (1).

Although it was possible to bring our converged $J_r = 0$ rigid-rotor CC calculations into agreement with the observed product state distributions by fine-tuning the strength of the Rb–KRb interaction, the resulting PES is extremely unlikely (Supplementary Information) and the observed total inelastic rate could still not be reproduced.

The lack of complete agreement between experiment and our scattering calculations using only the ground-state PES and the rigid-rotor approximation strongly suggests the importance of the KRb vibration and excited-state PES, which are the main missing elements in our theoretical model. This is supported by the presented *ab initio* calculations, which show that, at large R , the rigid-rotor assumption is a good approximation (the green and black lines overlap in Fig. 4a), while at short range, it is not due to the excited electronic state of Rb–KRb becoming energetically accessible. The related strong enhancement of spin–rotation coupling at the CI is shown in Fig. 4b. This enhancement correlates with the electron g -factor reaching zero, which can potentially lead to Majorana-type spin-flip transitions⁴⁵ at the CI. The CI could potentially introduce strong mixing between different J_r and explain the statistical distribution of the KRb rotational states.

Conclusion

Our experiment has demonstrated energy transfer from the atomic spin degree of freedom to molecular rotation in Rb ($|2, 2\rangle$) + KRb ($|0, 0, -4, 1/2\rangle$) collisions. Following collision, Rb predominantly populates a single hyperfine state ($|1, 1\rangle$) and KRb populates its various energetically allowed rotational levels up to $N = 2$. We experimentally observed interspecies spin-dependent hyperfine interactions. Intriguingly, our observations match well the statistical model under the assumption of the non-conservation of J_r . We developed a state-of-the-art quantum scattering methodology to understand the results. However, under the rigid-rotor assumption and using only the ground-state PES, the non-conservation of J_r cannot be justified and the quantitative branching ratio as well as the scattering cross-sections did not match the experiment after extensive efforts. In electronic structure calculations, we identified the enhancement of spin–rotation coupling close to the CI, which is energetically accessible and could play an important role in collision dynamics. As CIs can be found in a wide variety of molecules^{46,47}, the effect of the CI on spin-dependent interactions and the non-conservation of J_r can also be generalized to other chemical species and higher collision energies when the CI becomes more easily accessible. We note that fully converged scattering calculations that include vibrational modes and CIs are beyond the current state of the art^{42,43,48}. Our findings also shed light on a previously measured, exceptionally long lifetime of the ground-state Rb–KRb complex³⁴ that may have a similar origin. For the spin-state combination of KRb + Rb explored here, we measured the lifetime of the complex to be 0.54 ns (Supplementary Section D), while the calculated RRKM lifetime based on the ground-state electronic potential and neglecting the role of spin–rotation coupling is 0.6 ps. Properly taking into account nuclear spins and spin-dependent interactions could dramatically increase the density of states and may bring the RRKM estimate and experimental value to closer agreement. These joint experimental and theoretical efforts manifest the complexity of atom–molecule dynamics and call for more advanced theoretical and computational tools to study quantum scattering. One possible direction for future research could involve combining the CC methodology developed in this work

with rigorous quantum reactive scattering calculations that accurately account for the electronic, vibrational and rotational degrees of freedom of the collision partners^{42,43,48}.

Online content

Any methods, additional references, Nature Portfolio reporting summaries, source data, extended data, supplementary information, acknowledgements, peer review information; details of author contributions and competing interests; and statements of data and code availability are available at <https://doi.org/10.1038/s41557-025-01778-z>.

References

- Herschbach, D. R. Molecular dynamics of elementary chemical reactions (Nobel lecture). *Angew. Chem. Int. Ed. Engl.* **26**, 1221–1243 (1987).
- Lee, Y. T. et al. Molecular beam studies of elementary chemical processes (Nobel lecture). *Angew. Chem. Int. Ed. Engl.* **26**, 939–951 (1987).
- Wang, T. et al. Dynamical resonances in chemical reactions. *Chem. Soc. Rev.* **47**, 6744–6763 (2018).
- Zhao, B. & Guo, H. State-to-state quantum reactive scattering in four-atom systems. *Wiley Interdiscip. Rev. Comput. Mol. Sci.* **7**, e1301 (2017).
- Althorpe, S. C. & Clary, D. C. Quantum scattering calculations on chemical reactions. *Annu. Rev. Phys. Chem.* **54**, 493–529 (2003).
- Reberntrost, F. Electronic-to-rotational energy transfer in the system F + D₂. *Chem. Phys. Lett.* **58**, 18–22 (1978).
- Yuan, D. et al. Observation of the geometric phase effect in the H + HD → H₂ + D reaction. *Science* **362**, 1289–1293 (2018).
- Klein, A. et al. Directly probing anisotropy in atom–molecule collisions through quantum scattering resonances. *Nat. Phys.* **13**, 35–38 (2017).
- Dong, W. et al. Transition-state spectroscopy of partial wave resonances in the F + HD reaction. *Science* **327**, 1501–1502 (2010).
- de Jongh, T. et al. Imaging the onset of the resonance regime in low-energy NO–He collisions. *Science* **368**, 626–630 (2020).
- Krems, R. & Dalgarno, A. Electronic and rotational energy transfer in F(²P_{1/2}) + H₂ collisions at ultracold temperatures. *J. Chem. Phys.* **117**, 118–123 (2002).
- Alexander, M. H., Manolopoulos, D. E. & Werner, H.-J. An investigation of the F + H₂ reaction based on a full ab initio description of the open-shell character of the F(²P) atom. *J. Chem. Phys.* **113**, 11084–11100 (2000).
- Maussang, K., Egorov, D., Helton, J. S., Nguyen, S. V. & Doyle, J. M. Zeeman relaxation of CaF in low-temperature collisions with helium. *Phys. Rev. Lett.* **94**, 123002 (2005).
- Lara, M., Bohn, J. L., Potter, D., Soldán, P. & Hutson, J. M. Ultracold Rb–OH collisions and prospects for sympathetic cooling. *Phys. Rev. Lett.* **97**, 183201 (2006).
- Morita, M., Kosicki, M. B., Żuchowski, P. S. & Tschberbul, T. V. Atom-molecule collisions, spin relaxation, and sympathetic cooling in an ultracold spin-polarized Rb(²S)–SrF(²Σ) mixture. *Phys. Rev. A* **98**, 042702 (2018).
- Son, H., Park, J. J., Ketterle, W. & Jamison, A. O. Collisional cooling of ultracold molecules. *Nature* **580**, 197–200 (2020).
- Jurgilas, S. et al. Collisions between ultracold molecules and atoms in a magnetic trap. *Phys. Rev. Lett.* **126**, 153401 (2021).
- Walker, T. G. & Happer, W. Spin-exchange optical pumping of noble-gas nuclei. *Rev. Mod. Phys.* **69**, 629 (1997).
- Tschberbul, T. V., Zhang, P., Sadeghpour, H. R. & Dalgarno, A. Anisotropic hyperfine interactions limit the efficiency of spin-exchange optical pumping of ³He nuclei. *Phys. Rev. Lett.* **107**, 023204 (2011).
- Wang, X.-Y. et al. Magnetic Feshbach resonances in collisions of ²³Na⁴⁰K with ⁴⁰K. *New J. Phys.* **23**, 115010 (2021).
- Park, J. J. et al. Spectrum of Feshbach resonances in NaLi + Na collisions. *Phys. Rev. X* **13**, 031018 (2023).
- Bird, R. C., Tarbutt, M. R. & Hutson, J. M. Tunable Feshbach resonances in collisions of ultracold molecules in ²Σ states with alkali-metal atoms. *Phys. Rev. Res.* **5**, 023184 (2023).
- Park, J. J., Lu, Y.-K., Jamison, A. O., Tschberbul, T. V. & Ketterle, W. A Feshbach resonance in collisions between triplet ground-state molecules. *Nature* **614**, 54–58 (2023).
- Yang, H. et al. Creation of an ultracold gas of triatomic molecules from an atom–diatomic molecule mixture. *Science* **378**, 1009–1013 (2022).
- Tizniti, M. et al. The rate of the F + H₂ reaction at very low temperatures. *Nat. Chem.* **6**, 141–145 (2014).
- Yang, T. et al. Enhanced reactivity of fluorine with *para*-hydrogen in cold interstellar clouds by resonance-induced quantum tunnelling. *Nat. Chem.* **11**, 744–749 (2019).
- Mayle, M., Ruzic, B. P. & Bohn, J. L. Statistical aspects of ultracold resonant scattering. *Phys. Rev. A* **85**, 062712 (2012).
- Mayle, M., Quémener, G., Ruzic, B. P. & Bohn, J. L. Scattering of ultracold molecules in the highly resonant regime. *Phys. Rev. A* **87**, 012709 (2013).
- Christianen, A., Karman, T. & Groenenboom, G. C. Quasiclassical method for calculating the density of states of ultracold collision complexes. *Phys. Rev. A* **100**, 032708 (2019).
- Liu, Y. et al. Photo-excitation of long-lived transient intermediates in ultracold reactions. *Nat. Phys.* **16**, 1132–1136 (2020).
- Gregory, P. D., Blackmore, J. A., Bromley, S. L. & Cornish, S. L. Loss of ultracold ⁸⁷Rb¹³³Cs molecules via optical excitation of long-lived two-body collision complexes. *Phys. Rev. Lett.* **124**, 163402 (2020).
- Gersema, P. et al. Probing photoinduced two-body loss of ultracold nonreactive bosonic ²³Na⁸⁷Rb and ²³Na³⁹K molecules. *Phys. Rev. Lett.* **127**, 163401 (2021).
- Bause, R. et al. Collisions of ultracold molecules in bright and dark optical dipole traps. *Phys. Rev. Res.* **3**, 033013 (2021).
- Nichols, M. A. et al. Detection of long-lived complexes in ultracold atom–molecule collisions. *Phys. Rev. X* **12**, 011049 (2022).
- Bause, R., Christianen, A., Schindewolf, A., Bloch, I. & Luo, X.-Y. Ultracold sticky collisions: theoretical and experimental status. *J. Phys. Chem. A* **127**, 729–741 (2023).
- Jachymski, K., Gronowski, M. & Tomza, M. Collisional losses of ultracold molecules due to intermediate complex formation. *Phys. Rev. A* **106**, L041301 (2022).
- Tschberbul, T. V. & D’Incao, J. P. Ultracold molecular collisions in magnetic fields: efficient incorporation of hyperfine structure in the total rotational angular momentum representation. *Phys. Rev. A* **108**, 053317 (2023).
- Ni, K.-K. et al. A high phase-space-density gas of polar molecules. *Science* **322**, 231–235 (2008).
- Hu, M.-G. et al. Direct observation of bimolecular reactions of ultracold KRb molecules. *Science* **366**, 1111–1115 (2019).
- Schweiger, A. and Jeschke, G. *Principles of Pulse Electron Paramagnetic Resonance* (Cambridge Univ. Press, 2001).
- Aldegunde, J. & Hutson, J. M. Hyperfine structure of alkali-metal diatomic molecules. *Phys. Rev. A* **96**, 042506 (2017).
- Croft, J. et al. Universality and chaoticity in ultracold K + KRb chemical reactions. *Nat. Commun.* **8**, 15897 (2017).
- Kendrick, B. K. et al. Non-adiabatic quantum interference in the ultracold Li + LiNa → Li₂ + Na reaction. *Phys. Chem. Chem. Phys.* **23**, 5096–5112 (2021).
- Morita, M., Krems, R. V. & Tschberbul, T. V. Universal probability distributions of scattering observables in ultracold molecular collisions. *Phys. Rev. Lett.* **123**, 013401 (2019).
- Majorana, E. Atomi orientati in campo magnetico variabile. *Nuovo Cim.* **9**, 43–50 (1932).

46. Santoro, F. & Petrongolo, C. Nonadiabatic wave packet dynamics of NO₂ on the \tilde{X}^2/\tilde{X}^2 conical intersection. *J. Chem. Phys.* **110**, 4419–4427 (1999).
47. Yarkony, D. R. Diabolical conical intersections. *Rev. Mod. Phys.* **68**, 985–1013 (1996).
48. Morita, M. et al. Signatures of non-universal quantum dynamics of ultracold chemical reactions of polar alkali dimer molecules with alkali metal atoms: $\text{Li}(^2\text{S}) + \text{NaLi}(a^3\Sigma^+) \rightarrow \text{Na}(^2\text{S}) + \text{Li}_2(a^3\Sigma_u^+)$. *J. Phys. Chem. Lett.* **14**, 3413–3421 (2023).
49. Herzberg, G. *Spectra of Diatomic Molecules* (D. Van Nostrand, 1950)

Publisher's note Springer Nature remains neutral with regard to jurisdictional claims in published maps and institutional affiliations.

Springer Nature or its licensor (e.g. a society or other partner) holds exclusive rights to this article under a publishing agreement with the author(s) or other rightsholder(s); author self-archiving of the accepted manuscript version of this article is solely governed by the terms of such publishing agreement and applicable law.

© The Author(s), under exclusive licence to Springer Nature Limited 2025

Methods

Rb spin-flip rate based on a statistical model

We modelled the complex as a Rb atom repeatedly bouncing off the KRb molecule at average time intervals of Δt . By averaging over classical trajectories in a pure C_6 potential, Δt was previously estimated to be 1.0×10^{-10} s (ref. 27). While these mini-collisions are going on, the hyperfine constant of the Rb atom changes due to the presence of other atoms. The change from the native Rb hyperfine constant at large R to that at small R is given by $\Delta A = A^{FC}$ (ref. 36); it vanishes at large R and approaches a value $\Delta A \approx 1$ GHz at small R . Thus, the Rb atom sees its hyperfine constant fluctuate on a scale of ΔA at time intervals of roughly Δt . The probability (P) that a hyperfine transition may occur during a time T spent in the complex can be estimated according to²⁷:

$$P = \pi^2 \left(\frac{\Delta A \tau}{\hbar} \right) \left(\frac{\Delta A \Delta t}{\hbar} \right), \quad (2)$$

where \hbar is Planck's constant. Experimentally, we measured the intermediate complex lifetime to be $\tau = 0.54(10)$ ns (Supplementary Materials D), and thus the spin-flip probability is close to unity. This back-of-an-envelope estimation suggests that the transition can indeed be made on the observed timescale, while suggesting that a second transition, to $|10\rangle$, is less likely.

Statistical model of the KRb branching ratio

We proposed a statistical model as follows. We chose, in principle, a Jacobi coordinate system for the triatomic encounter. We let \mathbf{r} be the vector joining the K and Rb atoms in the molecule and \mathbf{R} the vector between the molecule's centre of mass and the incident Rb atom. Similar to the coupled-channel calculations, we assumed that the magnitude r is fixed, or more properly, that this degree of freedom is ignored. It may contribute to the lifetime of the complex or the density of resonant states, but it is unlikely to directly affect rotational branching ratios. Similarly, the magnitude R was not treated explicitly, except as follows: when R is large, the states of the system are given in terms of atom + molecule quantum numbers that define asymptotic $|a\rangle$ states, to be specified further in the following discussions; when R is small, the triatomic system is described by states $|c\rangle$ of the complex, also specified later.

Transitions between asymptotic states and states of the complex were handled in the spirit of a frame transformation. That is, the probability of a given incident asymptotic channel $|a\rangle$ finding itself in state $|c\rangle$ of the complex is $|\langle a|c\rangle|^2$, the matrix element taken over all degrees of freedom except R . Similarly, the same kind of matrix element gives the probability of complex channel $|c\rangle$ decaying into asymptotic channel $|a\rangle$.

For convenience, here we again identify the various angular momentum operators as follows: molecular rotation $\hat{\mathbf{N}}$, collision partial wave $\hat{\mathbf{L}}$, Rb atom nuclear spin $\hat{\mathbf{I}}_a$, Rb electronic spin $\hat{\mathbf{S}}$, K molecular nuclear $\hat{\mathbf{I}}_1$ is the spin and Rb molecular nuclear spin $\hat{\mathbf{I}}_2$. Using these ingredients, the separated atom–molecule states are given by

$$|a\rangle = |NM_N\rangle |LM_L\rangle |I_1 M_{I_1} I_2 M_{I_2}\rangle |F_a M_{F_a}\rangle, \quad (3)$$

where $|F_a M_{F_a}\rangle$ are the eigenstates of the square and z-projection of total atom angular momentum operators \hat{F}_a^2 and $\hat{F}_{a,z}$, $\hat{F}_a = \hat{\mathbf{S}} + \hat{\mathbf{I}}_a$ is the total angular momentum of the atom and M_L is the magnetic quantum number corresponding to L . The complex was assumed to be a state of good total angular momentum $|JM_J\rangle$, where M_J is the magnetic quantum number corresponding to J , in spite of the presence of small magnetic and electric fields. To describe the states of the complex, we chose the following angular momentum coupling scheme: molecular nuclear spin = $\hat{\mathbf{I}} = \hat{\mathbf{I}}_1 + \hat{\mathbf{I}}_2$; total spin = $\hat{\mathbf{F}} = \hat{\mathbf{I}} + \hat{\mathbf{S}}$; total mechanical rotation = $\hat{\mathbf{J}}_r = \hat{\mathbf{N}} + \hat{\mathbf{L}}$; total angular momentum = $\hat{\mathbf{J}} = \hat{\mathbf{J}}_r + \hat{\mathbf{F}}$. A state of the complex is therefore denoted

$$|c\rangle = |[(NL)J_r; (I_1 I_2)I; F_a] JM_J\rangle. \quad (4)$$

One further constraint on both basis sets is that parity be conserved, that is, $(-1)^{N+L} = 1$, as it is in the initial state with $N = L = 0$.

To determine overlap integrals for these states, we expanded the complex state explicitly as

$$|c\rangle = \sum_{\mathcal{M}} |NM_N\rangle |LM_L\rangle |I_1 M_{I_1} I_2 M_{I_2}\rangle |F_a M_{F_a}\rangle \quad (5)$$

$$\times \langle NM_N LM_L | J_r M_r \rangle \langle I_1 M_{I_1} I_2 M_{I_2} | IM_I \rangle \quad (6)$$

$$\times \langle IM_I F_a M_{F_a} | FM_F \rangle \langle J_r M_r FM_F | JM_J \rangle, \quad (7)$$

where $\mathcal{M} = \{M_r, M_F, M_N, M_L, M_I, M_{F_a}, M_{I_1}, M_{I_2}\}$ denotes, formally, the set of magnetic quantum numbers corresponding to $\{J_r, F, N, L, I, F_a, I_1, I_2\}$ in this expansion.

The projection of asymptotic states onto states of the complex therefore takes the form

$$\langle a|c\rangle = \langle NM_N LM_L | J_r M_r \rangle \langle I_1 M_{I_1} I_2 M_{I_2} | IM_I \rangle \quad (8)$$

$$\times \langle IM_I F_a M_{F_a} | FM_F \rangle \langle J_r M_r FM_F | JM_J \rangle. \quad (9)$$

Some of the quantum numbers are specified in the basis sets; others are determined by angular momentum conservation. Thus, $M_r = M_N + M_L$, $M_I = M_{I_1} + M_{I_2}$ and $M_F = M_J - M_r$.

In the initial state with $N = L = 0$, the overlap simplifies, as $J_r = 0$ and $J = F$. The probability of the initial complex finding itself in a state with total angular momentum J is the sum of the probabilities of arriving in any of the states with a given total J and all values of any other quantum numbers, in this case I . We denote this probability as follows:

$$P(J) = \sum_I |\langle I_1 M_{I_1} I_2 M_{I_2} | IM_I \rangle \langle IM_I F_a M_{F_a} | JM_J \rangle|^2, \quad (10)$$

where $M_{I_1} = -4$, $M_{I_2} = 1/2$ and $F_a = M_{F_a} = 2$ are specified by the initial condition.

It is likely that only certain substates of the complex, with a given value of JM_J , are populated by the initial collision, for example, only those with $N = L = 0$. In the full statistical approximation, it was assumed that the complex thoroughly scrambles all the states that are allowed by angular momentum conservation. That is, during the lifetime of the complex, all such states become equally populated. This assumption could be restricted later, based on other physical considerations.

In this circumstance, we considered the probability that the complex with total angular momentum J decays into an asymptotic channel where the molecule has rotation N . This is the sum of the probabilities $|\langle a|c\rangle|^2$ for all states of the complex with total angular momentum J and all final asymptotic channels consistent with N , summed over all the other quantum numbers. Such a probability ($D(N, J)$) is denoted

$$D(N, J) = \sum_{J_r, I, F} \sum_{M_N, L, M_r, M_L, M_I, M_{I_1}, M_{I_2}} |\langle NM_N LM_L | J_r M_r \rangle \langle I_1 M_{I_1} I_2 M_{I_2} | IM_I \rangle \quad (11)$$

$$\times \langle IM_I F_a M_{F_a} | FM_F \rangle \langle J_r M_r FM_F | JM_J \rangle|^2. \quad (12)$$

This expression requires $F_a = M_{F_a} = 1$ in the final state that is measured. The quantum numbers M_{I_1} and M_{I_2} are no longer constrained, but run over all allowed values.

The probability $D(N)$ that the incident state produces, after collision, a state of rotation N of the molecule is therefore the probability that a complex of total angular momentum J so decays, weighted by the probability that the collision populates such a complex in the first place, is given by:

$$D(N) = \sum_J P(J) D(N, J). \quad (13)$$

As noted earlier, the full statistical model would allow for all possible states of the complex. In particular, the mechanical rotation J_r could range over many values. In this case, the branching ratio for $N = 2, 1$ and 0 is $0.544:0.340:0.116$, in agreement with the measured results. However, as noted earlier, the available spin-rotation and tensor hyperfine interaction that can actually change J_r in a collision is quite weak, whereby we had to also consider incomplete statistical models that restrict the value of J_r . If J_r is completely restricted to its initial value of $J_r = 0$ (consistent with $N = L = 0$), then the unsuitable branching ratio $1:1:1$ results. However, if this weak perturbation can drive the complex from $J_r = 0$ to even $J_r = 2$, the corresponding statistical model restores the branching ratio to $0.50:0.33:0.17$. This suggests that only a weak scrambling is required to tip the complex into something like its full statistical behaviour.

1 + 1' REMPI detection of collisional products

Our scheme of the 1 + 1' REMPI detection of KRb used two lasers. One was a continuous-wave external cavity diode laser operating at 666 nm and the other was a pulsed frequency-doubled Nd:YVO₄ laser with a wavelength of 532 nm and a pulse duration of 10 ns. The 666 nm laser was resonant with the KRb X¹Σ⁺ ($v = 0$) to B¹Π ($v' = 0$) vibronic band transitions, as shown in Fig. 2. The power of the 666 nm light was 8.7 mW with a $1/e^2$ beam radius of 1.0 mm. The pulse energy of the 532 nm laser was set to 189 μJ with a $1/e^2$ beam radius of 1.0 mm. Similarly, the 1 + 1' REMPI detection of Rb used a continuous-wave external cavity diode laser operating at 420 nm and the same 532 nm pulsed laser. The 420 nm laser was resonant with the Rb 5S_{1/2}, $F = 1$ to 6P_{3/2} transitions, as shown in Fig. 2. The power of the 420 nm light was 1.9 mW with a $1/e^2$ beam radius of 1.0 mm. The REMPI beams were significantly larger than the ODT, which consisted of a horizontally propagating ODT beam and vertically propagating ODT beam with beam radii of 35 and 100 μm, respectively. This ensured that all post-collision products were exposed to the REMPI beams to maximize detection efficiency.

The 666 and 420 nm laser frequencies were stabilized by locking to a wavelength meter (Bristol 871A) inside a pressure-stable chamber. We further calibrated the wavelength meter readings to an external cavity diode laser at 970 nm locked to a high-finesse stable cavity, which enabled us to improve the frequency accuracy to 5 MHz.

To protect the reactant KRb molecules in the ODT from the scattering of the repeatedly fired REMPI pulses, we placed a copper wire (American Wire Gauge 36, 127-μm diameter) in the REMPI beam path and cast its shadow on the plane containing KRb molecules using an $f = 250$ mm focal length achromatic plano-convex lens. The shadow of the copper wire had a width of 250 μm and was centred around the location of the molecular cloud.

The 666 and 420 nm laser pulses were fired at a repetition rate of 10 kHz and temporally overlapped with the 532 nm pulses. The pulse lengths of the 666 and 420 nm light and the relative timings to the 532 nm pulses were controlled and optimized using a delay function generator. The resulting ions were accelerated onto an ion detector under a constant electric field ($E = 17$ V cm⁻¹) generated by a series of plate electrodes and counted^{39,50}. The ionization sequence lasted for 1 s, and the ODT intensity, magnetic field and electric field (perpendicular to the magnetic field) were held constant for the entire duration. The atoms and molecules were depleted after the ionization sequence.

From our KRb REMPI spectra (Fig. 2), we extracted rotational constants (B) of $2\pi \times 1,112(3)$ and $2\pi \times 961(1)$ MHz for KRb in the X¹Σ⁺ and B¹Π ($v' = 0$) states, which are in good agreement with the previously measured value³⁸ ($B = 2\pi \times 1,1139(1)$ GHz) and theoretical prediction⁵¹ ($B = 2\pi \times 953$ MHz). The Λ-doublet splitting of the B¹Π excited state is $2\pi \times 7(5)$ MHz. In addition, we observed that the frequency of the R(0) transition is offset by $2\pi \times 100$ MHz from the prediction using the rotational constants due to the light shift caused by the 532 nm light (Extended Data Fig. 1). It is important to take this into account to extract the population of post-collision $N = 0$ molecules.

We additionally checked the linear correlation between the product KRb molecule population and the initial $|2, 2\rangle$ Rb atom number (Extended Data Fig. 2), validating that the $N = 0$ KRb with sufficient kinetic energy to escape the ODT and the excited KRb molecules in $N = 1$ and 2 originate from inelastic atom-molecule collisions.

Monte Carlo simulation of REMPI

To obtain the branching ratio between different product rotational states, we created a model that accurately reflected the ionization efficiency for each state to convert the experimental signal ion counts to the corresponding molecule population. The model addressed several not-so-straightforward aspects, including the fact that the release of kinetic energy from the collision is small and the products could experience multiple ionization events in the detection volume. In addition, the 666 nm transition Rabi rate was comparable to the excited-state decay rate. As a consequence, a single ionization event could not deplete the ground-state population of the product molecules and later ionization events could also contribute to the total ion signal. Moreover, due to the Gaussian intensity profile of our REMPI beams, ionization events exhibited different dynamics depending on their distance from the trap centre.

To obtain an accurate branching ratio, we modelled all ionization processes through Monte Carlo (MC) simulations and fitted the data shown in Fig. 3 to our simulations.

In the simulations, both the 666 and 532 nm beams had Gaussian profiles with a $1/e^2$ beam radius of 1 mm. The width of the dark mask was 250 μm and covered the centre of the ionization beams. These geometric parameters were chosen to be consistent with our experimental values. Meanwhile, the three rotational states of the KRb product molecules had velocities of $v_0 = 4.18$ m s⁻¹, $v_1 = 3.54$ m s⁻¹ and $v_2 = 0.74$ m s⁻¹ for $N = 0, 1$ and 2 , respectively. The simulation was initialized with 1,000 product molecules for each rotational state, all located at the centre of the REMPI beams. Each molecule followed a uniform spherical velocity distribution and an initial starting time drawn from a uniform distribution between 0 and 100 μs, which was the time difference between two ionization events to model the asynchronous nature of product formation.

For every product molecule created with its initial time and velocity vector, the subsequent ionization process became deterministic. We calculated the coordinates of the molecules for each ionization pulse, from which we obtained the REMPI beam intensities for each ionization event. Each ionization event was modelled using a two-level system with decay in the excited state⁵². The dynamics of the ground state $|g\rangle$ in the X¹Σ⁺ manifold and the intermediate state $|e\rangle$ in the B¹Π can be described using the following rate equations:

$$\frac{d}{dt}\rho_{gg} = -\frac{i}{2}(\Omega_{ge}\rho_{eg} - \text{c.c.}), \quad (14)$$

$$\frac{d}{dt}\rho_{ee} = -(\Gamma + \Gamma_{\text{ion}})\rho_{ee} + \frac{i}{2}(\Omega_{ge}\rho_{eg} - \text{c.c.}), \quad (15)$$

$$\frac{d}{dt}\rho_{eg} = -\frac{1}{2}(\Gamma + \Gamma_{\text{ion}})\rho_{eg} + i\Delta\rho_{eg} + \frac{i}{2}\Omega_{eg}(\rho_{ee} - \rho_{gg}), \quad (16)$$

where c.c. represents the complex conjugate, ρ_{gg} and ρ_{ee} represent the populations in the ground and intermediate state, ρ_{eg} is the coherence between the two states, Ω_{ge} is the Rabi rate of the 666 nm bound-to-bound transition, Δ is the 666 nm laser detuning, Γ is the decay rate of the excited state $|e\rangle$ and Γ_{ion} is the ionization rate of the 532 nm bound-to-continuum transition. We characterized the decay rate of the excited state $\Gamma = 2\pi \times 15.6(3.2)$ MHz using absorption imaging and fixed this parameter in the MC simulation. The ion counts were calculated using $\int \rho_{ee}(t)\Gamma_{\text{ion}}(t)dt$, where $\Gamma_{\text{ion}}(t)$ is proportional to the 532 nm pulse intensity, with a peak value $\Gamma_{\text{ion}} = 2\pi \times 5$ MHz (ref. 52) at the centre of the Gaussian beam.

We solved the aforementioned rate equations for each ionization event and obtained the ion counts and remaining ground-state population ρ_{gg} , which rolls over to the next ionization event. We summed the ion counts from all product molecules and all ionization pulses that each molecule experienced, from which we extracted the branching ratio. We note that the choice of peak 532 nm laser ionization rate did not affect the final branching ratio. Doppler shifts were taken into account in our simulation.

When fitting the data to our MC simulation, we set the initial number of molecules, 666 nm Rabi rate and 666 nm laser detuning as free fitting parameters. Meanwhile, we fixed the excited-state decay rate, temporal profile of the REMPI pulses, the peak 532 nm laser ionization rate at the centre of the beam and the geometries of the REMPI beams with the dark line from experimentally measured values.

For the R(0) branch, we additionally took into account the light shift caused by the pulsed 532 nm light observed in the experiment by introducing a time-dependent detuning. We also considered the excited-state hyperfine structure in the R(0) transition (Extended Data Fig. 1) by extending the two-level system model to include three independent excited states with the same Rabi and decay rates. We did not observe significant light shifts in the Q(2) and Q(1) transitions caused by the 532 nm light. The hyperfine structures in the excited states in the Q(2) and Q(1) transitions are similar to R(0) and ignoring the hyperfine structure would cause at most a 5% overestimation of the excited-state population.

The fitted Rabi rates for Q(2), Q(1) and R(0) were $2\pi \times 10.2(2)$, $2\pi \times 10.0(5)$ and $2\pi \times 13.7(1.0)$ MHz, respectively, with the error bars representing a 68% confidence interval (Fig. 3). The R(0) Rabi rate extracted from the fitting agrees well with the Rabi rate measured using depletion spectroscopy ($2\pi \times 14(4)$ MHz). In addition, the ratio between the three Rabi rates shows good agreement with the Hönl–London factors⁵³ for $X^1\Sigma^+$ to $B^1\Pi$ transitions, assuming that the M_N distribution was randomized. In addition, no dependence of KRb ion counts on polarization was observed across all transitions, indicating that the M_N levels were scrambled after collision.

Data availability

The data supporting the findings of this study are available from the corresponding authors on request. Experimental data and related processing codes are also accessible at Harvard Dataverse via <https://doi.org/10.7910/DVN/O24MN4> (ref. 54).

References

50. Liu, Y., Grimes, D. D., Hu, M.-G. & Ni, K.-K. Probing ultracold chemistry using ion spectrometry. *Phys. Chem. Chem. Phys.* **22**, 4861–4874 (2020).
51. Borsalino, D. et al. Efficient optical schemes to create ultracold KRb molecules in their rovibronic ground state. *Phys. Rev. A* **90**, 033413 (2014).

52. Liu, Y. et al. Precision test of statistical dynamics with state-to-state ultracold chemistry. *Nature* **593**, 379–384 (2021).
53. Hansson, A. & Watson, J. K. A comment on Hönl–London factors. *J. Mol. Spectrosc.* **233**, 169–173 (2005).
54. Liu, Y., Zhu, L., Luke, J., Babin, M. C. and Ni, K.-K. Experimental data for hyperfine-to-rotational energy transfer in ultracold atom-molecule collisions. *Harvard Dataverse* <https://doi.org/10.7910/DVN/O24MN4> (2024).

Acknowledgements

We thank M. Frye, Y. Liu, J. Zhang, Z. Li and A. Houwman for helpful discussions. The experimental team (Y.-X.L., L.Z., J.L., M.C.B. and K.-K.N.) was supported by the US Department of Energy (DOE), Office of Science, Basic Energy Sciences (award no. DE-SC0024087; molecule state detection), the Center for Ultracold Atoms (an NSF Physics Frontiers Center, PHY-2317134; atom state detection) and AFOSR DURIP FA9550-23-1-0122 (instrument upgrade). The Warsaw team (M.G., H.L. and M.T.) acknowledges the European Union (ERC, 101042989, QuantMol) and the PL-Grid Infrastructure (grant no. PLG/2023/016115). T.V.T. gratefully acknowledges support from the NSF CAREER program (grant no. PHY-2045681). J.L.B. acknowledges support from the JILA Physics Frontier Center (PHY-2317149).

Author contributions

Y.-X.L., L.Z., J.L., M.C.B. and K.-K.N. carried out the experimental work and data analysis. T.V.T. carried out the coupled-channel calculations. M.G., H.L. and M.T. performed the ab initio calculations of the Rb+KRb interactions. J.L.B. developed the statistical model of the KRb branching ratio. All authors contributed to the interpretation of the results and writing of the paper.

Competing interests

The authors declare no competing interests.

Additional information

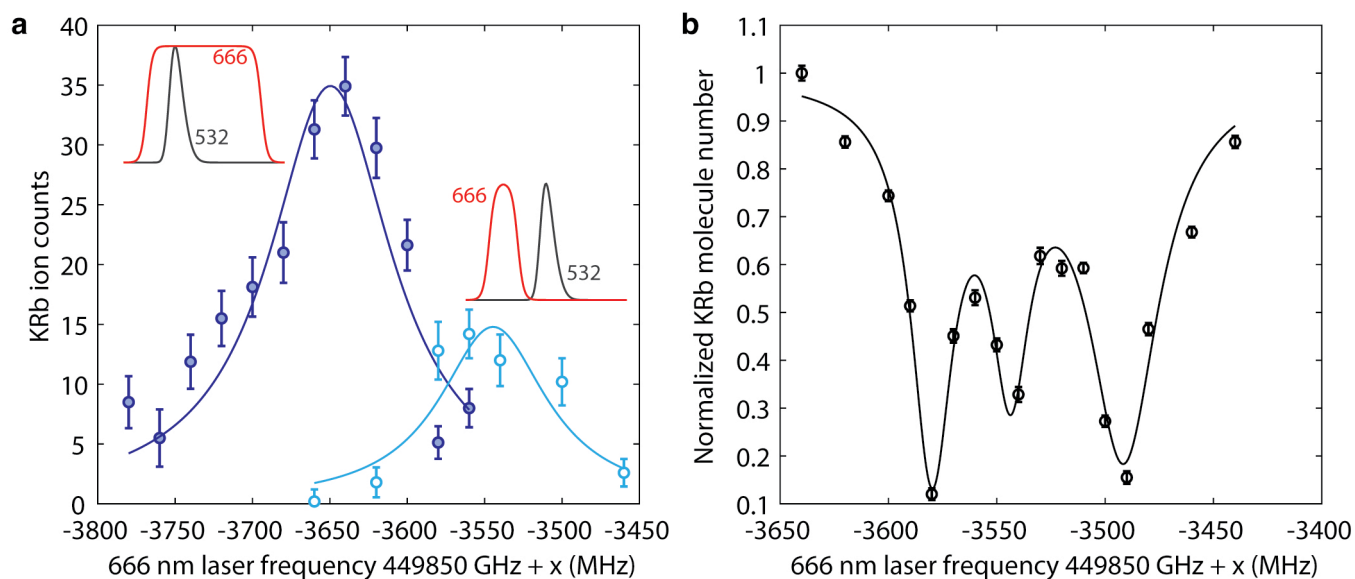
Extended data is available for this paper at <https://doi.org/10.1038/s41557-025-01778-z>.

Supplementary information The online version contains supplementary material available at <https://doi.org/10.1038/s41557-025-01778-z>.

Correspondence and requests for materials should be addressed to Kang-Kuen Ni.

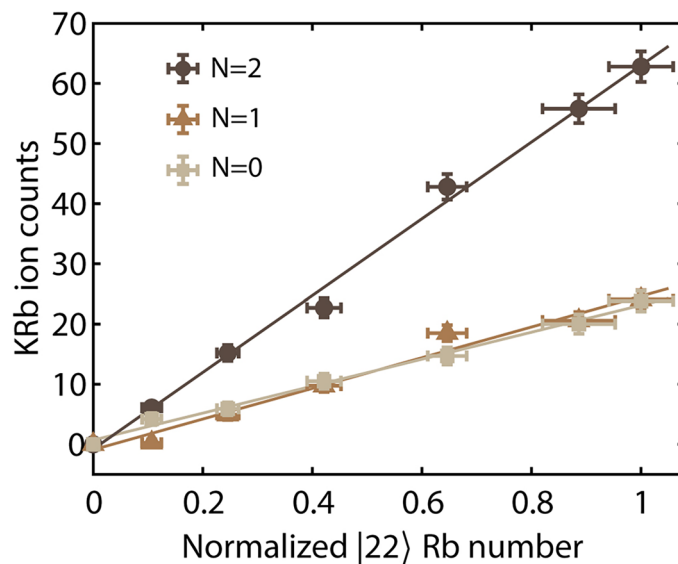
Peer review information *Nature Chemistry* thanks the anonymous reviewers for their contribution to the peer review of this work.

Reprints and permissions information is available at www.nature.com/reprints.



Extended Data Fig. 1 | Light shift and hyperfine structure observed in the R(0) transition. (a) Pulsed 532 nm light induced light shift in the R(0) transition. The dark blue solid circles represent the R(0) transition with an overlapping 666 nm pulse and 532 nm pulse. The light blue open circles represent the R(0) transition without overlapping 666 nm and 532 nm pulses. The solid lines are fittings to Lorentzian lineshapes. The insets are the corresponding REMPI pulse timing

diagrams. The data were collected using 5 averages. (b) Depletion spectroscopy of $N=0$ KRb molecules from absorption imaging near R(0) transitions. The spectrum shows hyperfine structure of the $N=1$ level in the electronically excited state. The data points represent the mean value, normalized to the maximum molecule number. All error bars in this figure represent the shot noise.



Extended Data Fig. 2 | Rb atom number dependence of KRb ion counts. KRb ion counts were measured with the 666 nm laser resonant with the Q(2) (circles), Q(1) (triangles) and R(0) (squares) transitions as a function of the initial $|2, 2\rangle$ Rb atom number, which was controlled by varying the duration of the microwave ARP pulse. To account for imperfections in the dark mask that give rise to signal from $|1, 1\rangle$ atoms in the reactant cloud, the same measurements were performed

without a microwave ARP pulse to establish a background. The results with background subtraction are shown here. For each point, the X-axis values and error bars indicate the mean and standard deviation of relative atom number of the 5 measurements, while Y-axis values and error bars represent the mean of 5 measurements and shot noise. Solid lines are linear fits to the data.

Extended Data Table 1 | Table of product KRb branching ratio under different conditions. We presented 30 G, $|2, 2\rangle$ Rb + N=0 KRb data in the main text. Electric fields for all three datasets are the same (17 V/cm and perpendicular to the magnetic field)

Condition	N=2	N=1	N=0
2 G, $ 2, 2\rangle$ Rb + N=0 KRb	0.54(9)	0.36(7)	0.10(2)
30 G, $ 2, 2\rangle$ Rb + N=0 KRb	0.53(9)	0.33(8)	0.13(3)
30 G, $ 2, 2\rangle$ Rb + N=1 KRb	0.59(13)	0.32(9)	0.09(2)